

Accepted Manuscript

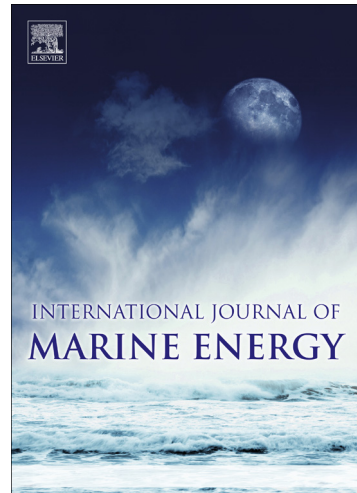
Comparative turbulent three-dimensional Navier-Stokes hydrodynamic analysis and performance assessment of oscillating wings for renewable energy applications

Jernej Drolfelnik, Sergio Campobasso

PII: S2214-1669(16)30043-1

DOI: <http://dx.doi.org/10.1016/j.ijome.2016.05.009>

Reference: IJOME 115



To appear in:

Please cite this article as: J. Drolfelnik, S. Campobasso, Comparative turbulent three-dimensional Navier-Stokes hydrodynamic analysis and performance assessment of oscillating wings for renewable energy applications, (2016), doi: <http://dx.doi.org/10.1016/j.ijome.2016.05.009>

This is a PDF file of an unedited manuscript that has been accepted for publication. As a service to our customers we are providing this early version of the manuscript. The manuscript will undergo copyediting, typesetting, and review of the resulting proof before it is published in its final form. Please note that during the production process errors may be discovered which could affect the content, and all legal disclaimers that apply to the journal pertain.

Comparative turbulent three-dimensional Navier-Stokes hydrodynamic analysis and performance assessment of oscillating wings for renewable energy applications

Jernej Drofelnik^a, Sergio Campobasso^{b,*}

^a*University of Glasgow, School of Engineering. James Watt Building South, University Avenue, Glasgow G12 8QQ, United Kingdom.*

^b*University of Lancaster, Department of Engineering. Engineering Building, Gillow Avenue, Lancaster LA1 4YW, United Kingdom.*

Abstract

Oscillating wings can extract energy from an oncoming water or air stream, and first large-scale marine demonstrators are being tested. Oscillating wing hydrodynamics is highly unsteady, may feature dynamic stall and leading edge vortex shedding, and is significantly three-dimensional due to finite-wing effects. Understanding the interaction of these phenomena is essential for maximizing power generation efficiency. Much of the knowledge on oscillating wing hydrodynamics stemmed from two-dimensional low-Reynolds number computational fluid dynamics studies and laboratory testing; real installations, however, will feature Reynolds numbers higher than 1 million and unavoidable finite-wing-induced losses. This study investigates the impact of flow three-dimensionality on the hydrodynamics and the efficiency of a realistic aspect ratio 10 device in a stream with Reynolds number of 1.5 million. The improvements achievable by using endplates to reduce finite-wing-induced losses are also analyzed. Three-dimensional time-dependent Navier-Stokes simulations using the shear stress transport turbulence model and a 30-million-cell grid are performed. Detailed comparative hydrodynamic analyses of the finite and the infinite wings reveal that flow three-dimensionality reduces the power generation efficiency of the

*Corresponding author

Email addresses: j.drofelnik.1@research.gla.ac.uk (Jernej Drofelnik), m.s.campobasso@lancaster.ac.uk (Sergio Campobasso)

finite wing with sharp tips and that with endplates by about 17 % and 12 % respectively. Presented analyses suggest approaches to further reducing these power losses.

Keywords: Energy-extracting oscillating wing, Finite wing effects, Leading edge vortex shedding, Turbulent Navier-Stokes CFD

1. Introduction

Increasing demand for electricity production and stricter environmental policy have greatly contributed to the development of novel renewable energy generation systems. A promising concept in the fields of wind and tidal energy systems relies on the use of oscillating wings simultaneously heaving and pitching to extract energy from an oncoming water or air stream. The concept was pioneered by McKinney and DeLaurier [1] in 1981, and further investigated by Jones *et al.* [2]. Several other numerical, experimental and prototype-based studies of the oscillating wing device for power generation followed these pioneering studies. Recently Young *et al.* [3] published a comprehensive review of the analytical, numerical and experimental research work carried out in this field. The review also focuses on the influence of flapping kinematics and foil geometry parameter choice on the characteristics of the leading edge vortex shedding observed in certain operating conditions. This feature has been initially thought to have a beneficial effect on the efficiency of the energy generation of oscillating wings, and its analysis in realistic installations is one of the underlying threads of the present study. The authors of the article [3] also highlight outstanding questions on the fluid mechanics of the oscillating wing in real installations, characterized by high values of the Reynolds number based on the foil chord and the freestream velocity, and complex three-dimensional (3D) flow features. The kinematic set-ups of oscillating wings for power generation can be subdivided in three classes [3, 4]: fully active, semi-passive and fully passive. In the fully active set-up all parameters of the heaving and pitching motions are prescribed; in the semi-passive set-up only the pitching motion is prescribed and

the heaving motion parameters are determined by the hydrodynamic forces acting on the wing; in the fully passive arrangement, both the pitching and heaving motion parameters are determined by the forces acting on the wing. To date, it is still unclear which of the three set-ups provides the best performance [3], but progress made on improving the understanding of the hydrodynamic characteristics of any one of the three set-ups is likely to contribute to progress in the study and application of the other two [4]. The wing oscillation considered in most analyses is harmonic, but it has been shown that performance benefits can also be achieved by considering non-harmonic wing trajectories [5, 6]. The remainder of the literature survey in this section and the analyses in this paper focus on the baseline configuration of the oscillating wing, namely that using a fully active kinematic set-up and harmonic wing motion.

Kinsey and Dumas [7] performed a thorough parametric computational fluid dynamics (CFD) investigation into the dependence of the energy conversion efficiency of a foil oscillating in a laminar Reynolds 1,100-stream on the choice of motion parameters (heaving and pitching amplitude and motion frequency) and foil characteristic parameters (foil thickness and location of pitching axis). Their study used the commercial CFD code FLUENT and concluded that, by suitably choosing motion frequency and pitching amplitude, efficiencies as high as 34 % could be obtained. They also reported that the main factor enabling this efficiency level is the achievement of an optimal synchronization (or phase) of wing motion and unsteady leading edge vortex shedding (LEVS) associated with the dynamic stall observed for certain choices of foil trajectory parameters. Similar findings were also reported in a later independent study using the Navier-Stokes (NS) research code COSA [8].

An experimental 2 kW prototype of the oscillating wing for power generation was designed, built and tested by Laval University in water at Lac-Beauport near Quebec City. Measured data confirmed fairly high values of the energy conversion efficiency [9]. In the experiment, both a two-wing tandem configuration and a single-wing configuration were tested. The wings had aspect ratio (AR) 7, their tips featured endplates and the Reynolds number was 0.5 million.

Thereafter, the hydrodynamics of the devices tested at Lac-Beauport was investigated numerically by Kinsey and Dumas [10]. Both two-dimensional (2D) and 3D turbulent FLUENT simulations using the Spalart-Allmaras turbulence model [11] were performed. The study highlighted that the loss of power generation efficiency of a single $AR = 7$ wing with endplates in a water stream with $Re = 0.5 \times 10^6$ is about 15 % of the efficiency of the infinite wing. In a follow-up study, the same authors extended their numerical analyses to wings of $AR = 5, 7$ and 10 with and without endplates to assess the dependence of the losses induced by finite-wing effects on aspect ratio and wing tip type setting again $Re = 0.5 \times 10^6$. Making use of FLUENT simulations based on 3D grids with up to 3.5 million cells and using the Spalart-Allmaras model for the turbulence closure, their investigations concluded that, for a finite wing of $AR \geq 10$ with endplates such a loss could be limited to about 10 % of the efficiency of the infinite wing [12]. For the $AR = 10$ case, however, no simulation of the wing without endplates was performed, and therefore, it was not possible to assess separately the efficiency improvement due to the use of endplates and that due to the use of a fairly large and more realistic $AR = 10$.

The dependence of the oscillating wing hydrodynamics on the Reynolds number is another crucial factor essential to maximizing the energy extraction efficiency of future real installations. Cross-comparison of laminar low-Reynolds number and turbulent high-Reynolds number CFD simulations using the same wing motion parameters reveals that such efficiency is significantly higher in the latter regime [7, 10, 13]. This was reported by the authors of this paper who used COSA to carry out a 2D fully laminar Reynolds 1,100-simulation [8] and a 2D fully turbulent Reynolds 1.5 million-simulation [13] of the oscillating wing using the same wing motion parameters for both regimes. The comparative analysis reported in [13] used a wing trajectory that had been previously optimized for maximum energy extraction efficiency in the considered laminar regime, and provided two important observations. Firstly, the wing power generation efficiency increased at the turbulent high Reynolds number regime due primarily to thinner boundary layers, resulting in thinner effective foil and thus

larger lift forces. Secondly, LEVS was delayed in the turbulent high Reynolds number regime with respect to the laminar low Reynolds number regime due to higher stability of the turbulent boundary layers. Thus the optimal synchronization of wing motion and LEVS of the laminar regime was reduced in the high-Reynolds number case. However, the beneficial effect of thinner turbulent boundary layers outweighed the detrimental effect of abovesaid reduction of optimal synchronization, resulting in higher efficiency of the foil in the turbulent stream. It was assumed that, for high Reynolds number regimes, resetting an optimal synchronization of wing motion and LEVS by suitably varying the trajectory parameters could lead to an efficiency level even higher than that of 40 % obtained for the considered turbulent regime. However, Kinsey and Dumas later showed that high power generation efficiency at high Reynolds numbers does not necessarily rely on the occurrence of LEVS [14].

The interest of the industrial and scientific communities in the oscillating wing device keeps growing, as also highlighted by the installation of the 1.2 MW prototype of Pulse Tidal in the Bristol Channel in 2014 [3]. However, significant uncertainty on the impact of 3D flow features on the power generation efficiency of future real installations still exists, particularly at the expectedly high Reynolds numbers. This study focuses on the hydrodynamics of *AR* 10 oscillating wings without and with endplates at a realistic Reynolds number of 1.5 million. Close-to-optimal wing motion parameters, based on reported 2D CFD analyses [14], are used. The investigation aims at assessing the level and the mechanisms of the power generation efficiency loss, estimating the efficiency improvements due to the use of endplates for the considered aspect ratio, and highlighting a new route to further efficiency improvement of a wing with endplates. The investigation is based on 3D time-dependent (*TD*) Reynolds-averaged Navier-Stokes simulations based on a 30.7 million cell-grid and using Menter's shear stress transport turbulence model [15].

The paper starts with the definition of the kinematic and dynamic parameters of the oscillating wing motion. This is followed by the definition of the governing equations and a brief description of the COSA NS research code used

in this study. A detailed comparative analysis of the infinite and finite span wings in turbulent flow conditions is then reported, examining, discussing and quantifying the differences of unsteady hydrodynamic characteristics of the considered wing configurations. A summary of the main findings and concluding remarks are provided in the closing section.

2. Oscillating wing device

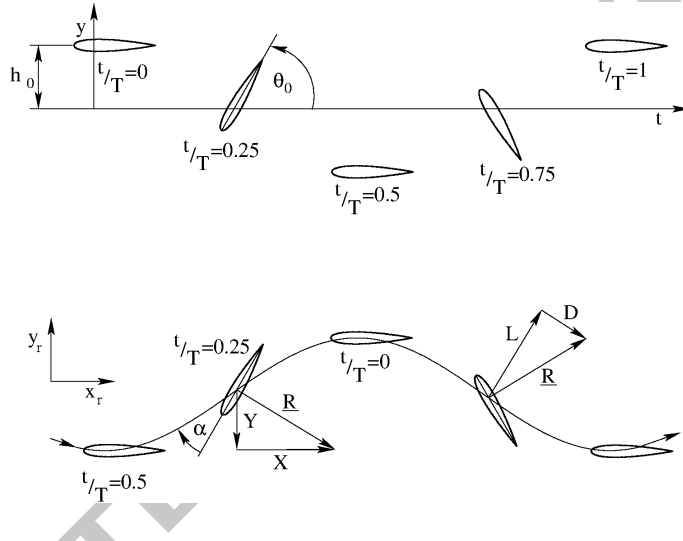


Figure 1: Top: prescribed motion of oscillating wing for power generation. Bottom: foil motion in reference system moving with freestream velocity.

Here an oscillating wing is defined as a foil experiencing simultaneous pitching $\theta(t)$ and heaving $h(t)$ motions. The following mathematical representation of the imposed motion is that adopted in [7]. Taking a pitching axis located on the chord line at position x_p from the leading edge (LE), the foil motion is expressed as:

$$\theta(t) = \theta_0 \sin(\omega t) \rightarrow \Omega(t) = \theta_0 \omega \cos(\omega t) \quad (1)$$

$$h(t) = h_0 \sin(\omega t + \phi) \rightarrow v_y(t) = h_0 \omega \cos(\omega t + \phi) \quad (2)$$

where θ_0 and h_0 are respectively the pitching and heaving amplitudes, Ω is the
¹³⁰ pitching velocity, v_y is the heaving velocity, ω is the angular frequency and ϕ is
 the phase between heaving and pitching. In this study, ϕ is set to 90° , and the
 NACA0015 foil is selected. The freestream velocity is denoted by u_∞ and the
 angular frequency ω is linked to the vibration frequency f by the relationship
 $\omega = 2\pi f$. The prescribed oscillating motion is depicted in the top sketch of
¹³⁵ Fig. 1.

An oscillating symmetric foil can operate in two different regimes: propulsive
 or power-extracting mode. This distinction originates from the sign of the forces
 that the flow generates on the oscillating foil. Based on the imposed motion and
 the upstream flow conditions, the foil experiences an effective angle of attack
¹⁴⁰ (AoA) α and an effective velocity v_e given respectively by:

$$\alpha(t) = \arctan(-v_y(t)/u_\infty) - \theta(t) \quad (3)$$

$$v_e(t) = \sqrt{u_\infty^2 + v_y(t)^2} \quad (4)$$

The maximum values of α and v_e have a major impact on the amplitude of
 the peak forces in the cycle, and also on the occurrence of dynamic stall. The
 maximum effective AoA reached in the cycle is approximated by the modulus of
 its quarter-period value, that is $\alpha_{max} \approx |\alpha(T/4)|$. As explained in [7], the power-
¹⁴⁵ extracting regime (in a mean sense, over one cycle) occurs when $\alpha(T/4) < 0$.
 This condition is represented in the bottom sketch of Fig. 1, which provides a
 time-sequence viewed in a reference frame moving with the farfield flow at u_∞ ,
 so that the effective AoA $\alpha(t)$ is made visible from the apparent trajectory of the
¹⁵⁰ foil. In this sketch, the resultant force R is first constructed from typical lift and
 drag forces (right-hand side) and then decomposed into X and Y components
 (left-hand side). One sees that the vertical force component Y is in phase with
 the vertical velocity component v_y of the foil over the entire cycle. This implies
 that the wing extracts energy from the fluid as long as no energy transfer asso-
 ciated with the component X of the hydrodynamic force takes place. This is the
¹⁵⁵ case since the foil does not move horizontally. The hydrodynamic phenomena
 occurring during the wing oscillation are substantially more complex than the

quasi-steady model discussed above. In some cases, for example, the efficiency of the energy extraction was shown to be heavily influenced by the occurrence of unsteady leading edge vortex shedding (LEVS) associated with dynamic stall
 160 and the phase between LEVS and foil kinematics.

The instantaneous power extracted from the flow is the sum of a heaving contribution $P_y(t) = Y(t)v_y(t)$ and a pitching contribution $P_\theta(t) = M(t)\Omega(t)$, where M denotes the hydrodynamic torque acting on the wing computed about the wing axis through the pitching center x_p . Denoting by c the foil chord,
 165 and z the coordinate along the wing span with origin at midspan, the power coefficient per unit wing length at position z is defined as:

$$C_{P_z}(t) \equiv P_z / (\frac{1}{2}\rho_\infty u_\infty^3 c) \quad (5)$$

where P_z is the sum of the instantaneous pitching and heaving power per unit wing length. The overall power coefficient, *i.e.* the nondimensional expression of the overall power extracted by the entire wing at time t is instead:

$$C_P(t) = \frac{1}{2l} \int_{-l}^l C_{P_z} dz \quad (6)$$

170 where l denotes the wing semispan. Introducing the time-dependent heaving force coefficient $C_Y(t)$ and pitching moment coefficient C_M , defined respectively as $C_Y(t) = Y(t)/[\frac{1}{2}\rho_\infty u_\infty^2 c(2l)]$ and $C_M(t) = M(t)/[\frac{1}{2}\rho_\infty u_\infty^2 c^2(2l)]$, the nondimensional mean power produced over one cycle can be written as:

$$\bar{C}_P = \bar{C}_{P_y} + \bar{C}_{P_\theta} = \frac{1}{T} \int_0^T \left[C_Y(t) \frac{v_y(t)}{u_\infty} + C_M(t) \frac{\Omega(t)c}{u_\infty} \right] dt \quad (7)$$

In the analyses reported below, use is also made of the heaving power coefficient per unit wing length $C_{P_{zy}}$ and the pitching power coefficient per unit wing length $C_{P_{z\theta}}$, obtained respectively by replacing P_z in Eqn. (5) with the instantaneous pitching and heaving power per unit wing length. Similarly, the time-dependent heaving power coefficient C_{P_y} and pitching power coefficient C_{P_θ} are obtained respectively by replacing C_{P_z} in Eqn. (6) with $C_{P_{zy}}$ and $C_{P_{z\theta}}$. For
 175 2D problems, the expression of the time-dependent overall power coefficient C_P is provided by Eqn. (5), and the heaving and pitching power coefficient are
 180

computed using the same equation but considering separately the heaving and pitching power components.

The efficiency η of the power generation process is here defined as the ratio of the extracted mean power $\bar{P} = \frac{1}{2}\bar{C}_P\rho_\infty u_\infty^3 c(2l)$ and the total available power $P_a = \frac{1}{2}\rho_\infty u_\infty^3 d(2l)$ in the oncoming flow passing through the swept area (the flow window):

$$\eta \equiv \frac{\bar{P}}{P_a} = \bar{C}_P \frac{c}{d} \quad (8)$$

where d is the overall vertical extent of the foil motion. This distance depends on the heaving and pitching motion parameters h_0 , θ_0 and ϕ . The power extraction efficiency η defined by Eq. (8) corresponds to the classical power coefficient obtained by means of Betz's analysis [16], which shows that the upper limit of η is $16/27 \times 100 \approx 59.3\%$. Therefore, Eq. (8) provides the relationship between the mean power coefficient \bar{C}_P defined by Eq. (7) and Betz's theory power coefficient (η).

195 3. Navier-Stokes CFD solver

The finite volume structured multi-block compressible Reynolds-averaged NS (RANS) code COSA [8, 13, 17] uses Menter's shear stress transport (SST) turbulence model [15]. Given a moving control volume \mathcal{C} with time-dependent boundary $S(t)$, the Arbitrary Lagrangian-Eulerian integral form of the system 200 of the time-dependent RANS and SST equations is:

$$\frac{\partial}{\partial t} \left(\int_{\mathcal{C}(t)} \mathbf{U} d\mathcal{C} \right) + \oint_{S(t)} (\underline{\Phi}_c - \underline{\Phi}_d) \cdot d\underline{S} - \int_{\mathcal{C}(t)} \mathbf{S} d\mathcal{C} = 0$$

The array \mathbf{U} of conservative flow variables is defined as: $\mathbf{U} = [\rho \underline{\mathbf{v}}^T \rho E \rho k \rho \omega]^T$ where ρ and $\underline{\mathbf{v}}$ are respectively the fluid density and velocity vector, and E , k and ω are respectively the total energy, the turbulent kinetic energy and the specific dissipation rate of turbulent kinetic energy, all per unit mass. The perfect gas equation is used to link internal energy, pressure and density. The generalized convective flux vector $\underline{\Phi}_c$ depends on \mathbf{U} and the velocity of the boundary S . The generalized diffusive flux vector $\underline{\Phi}_d$ depends primarily on the

sum of the molecular stress tensor, proportional to the strain rate tensor $\underline{\underline{s}}$, and the turbulent Reynolds stress tensor. Adopting Boussinesq's approximation, the latter tensor is also proportional to $\underline{\underline{s}}$ through an eddy viscosity μ_T . In the SST model, μ_T depends on ρ , k , ω and the vorticity.

The only nonzero entries of the source term \mathbf{S} are those of the k and ω equations, given respectively by:

$$\begin{aligned} S_k &= \mu_T P_d - \frac{2}{3}(\nabla \cdot \underline{\underline{v}})\rho k - \beta^* \rho k \omega \\ S_\omega &= \gamma \rho P_d - \frac{2}{3}(\nabla \cdot \underline{\underline{v}}) \frac{\gamma \rho k}{\nu_T} - \beta \rho \omega^2 + CD_\omega \end{aligned}$$

with

$$\begin{aligned} P_d &= 2 \left[\underline{\underline{s}} - \frac{1}{3} \nabla \cdot \underline{\underline{v}} \right] \nabla \underline{\underline{v}} \\ CD_\omega &= 2(1 - F_1) \rho \sigma_{\omega 2} \frac{1}{\omega} \nabla k \cdot \nabla \omega \end{aligned}$$

where $\nu_T = \mu_T / \rho$, $\sigma_{\omega 2}$ is a constant, F_1 is a flow state-dependent function, and σ_k , σ_ω , γ , β^* and β are weighted averages of corresponding constants of the standard $k-\omega$ and $k-\epsilon$ models with weights F_1 and $(1 - F_1)$, respectively [15].

COSA is second order accurate in time and space, and uses a very efficient MPI parallelization [18]. The accuracy of the space- and time-discretization has been thoroughly validated by considering a wide set of analytical and experimental test cases [8, 13, 17].

4. Results

Thorough investigations into the 3D hydrodynamics of oscillating wings for power generation are reported herein. Most analyses are based on 3D time-accurate RANS simulations performed with COSA. The physical and computational set-up of all simulations is described first. Thereafter the 3D unsteady flow mechanisms accounting for the variations of the energy capture moving from the ideal scenario of an infinite wing to the realistic case of a finite wing are analyzed. Moreover, the dependence of the 3D flow patterns and, ultimately, of the energy capture efficiency on the wing tip geometry is carefully examined.

4.1. physical and numerical set-up

The selected wing profile is the NACA0015 foil. The wing trajectory features a heaving and a pitching motion component defined by Eqs. (1) and (2) respectively. The operating condition characterized by a high efficiency of the energy extraction in the turbulent flow regime described in [13] (case A) is considered. The heaving amplitude h_0 equals one chord and the pitching center is at $x_p = 1/3$ of the chord from the LE. The pitching amplitude θ_0 is 76.3° and the phase angle ϕ between heaving and pitching motions is 90.0° . This parameter choice yields a value of the overall height h swept by the foil of 2.56 chords. The nondimensionalized frequency $f^* = fc/u_\infty$ is 0.14, where f is the frequency in Hertz, and the Reynolds number $Re = u_\infty c/\nu$, with ν being the kinematic viscosity, is 1.5×10^6 .

The time-dependent 3D turbulent flow fields past the oscillating wing were computed using structured multi-block non-deforming moving grids. In all simulations the entire grid moved rigidly with the wing. The 3D grid was obtained by extruding the 2D grid past the foil in the spanwise direction. The node coordinates of 2D and 3D grids were nondimensionalized by the foil chord.

The required level of spatial refinement of the 3D grid in the foil plane was assessed by means of 2D simulations using 256 time-intervals per oscillation cycle. More specifically, the periodic 2D flow field associated with the motion and flow parameters reported above was computed using four O-grids: one of dimension 256×256 (coarse) with 256 intervals on the foil and 256 intervals in the normal-like direction, and the other three of dimensions 512×512 (medium), 1024×1024 (fine), and 2048×2048 (extrafine). In all cases, the farfield boundary in the foil plane was at about 50 chords from the foil. On the extrafine grid level, the distance d_w of the first grid points off the foil surface from the foil itself was about $8 \times 10^{-7}c$. The fine grid was obtained from the extrafine by removing every second line in both directions, and this approach was used recursively to also obtain the medium and coarse level grids. The periodicity error of the 2D simulations using these four grids and all other simulations of this study was assessed by monitoring the evolution of the heaving force coefficient C_Y . The

simulations were run until the maximum difference between C_Y over the last two oscillation cycles became about 0.1 % of the maximum value of C_Y over the last cycle. It was chosen to monitor the periodicity error of C_Y because
²⁶⁵ the vertical force component gives the highest contribution to the extracted power. The periodic profiles of the overall power coefficient C_P , the heaving power coefficient C_{P_y} and the pitching power coefficient C_{P_θ} resulting from the mesh refinement assessment are reported respectively in the top, middle and bottom subplot of Fig. 2. The number 256 following the acronym *TD* indicates
²⁷⁰ the number of time steps per period. It is noted that some relatively small differences among the four C_P profiles exist in the first 10 % of the semi-period, and that such differences become progressively smaller as the grid refinement is increased. The same observation also holds for the four C_{P_y} profiles. These
²⁷⁵ discrepancies are caused by small variations of the phase of the LEVS associated with the considered regime [13] with respect to the foil oscillation. This occurrence is highlighted by the notable dependence of the position of the sharp peak of C_{P_θ} on the level of spatial refinement. As expected, these variations decrease as the grid is refined, become very small when passing from the fine to the extrafine grid refinement, indicating that the 1024×1024 grid provides a
²⁸⁰ fairly grid-independent solution. The mean values of the power coefficient profiles depicted in Fig. 2 are reported in Tab. 1, which also provides the efficiency η defined by Eqn. (8). One sees that the output featuring the highest sensitivity to the spatial refinement is the mean pitching power. Due to significantly higher levels of heaving power, however, the variability of the overall mean power and
²⁸⁵ the efficiency is significantly smaller.

To assess the solution sensitivity to the level of temporal refinement, the selected regime was simulated with the coarse-refinement grid using a number of time-intervals per period N_T of 128, 256, 512 and 1024. The periodic profiles of C_P , C_{P_y} and C_{P_θ} obtained with these four simulations are reported respectively in the top, middle and bottom subplot of Fig. 3. Similarly to the case of the spatial refinement, some relatively small differences among the four C_P profiles and among the four C_{P_y} profiles exist in the first 10 % of the semi-period.
²⁹⁰

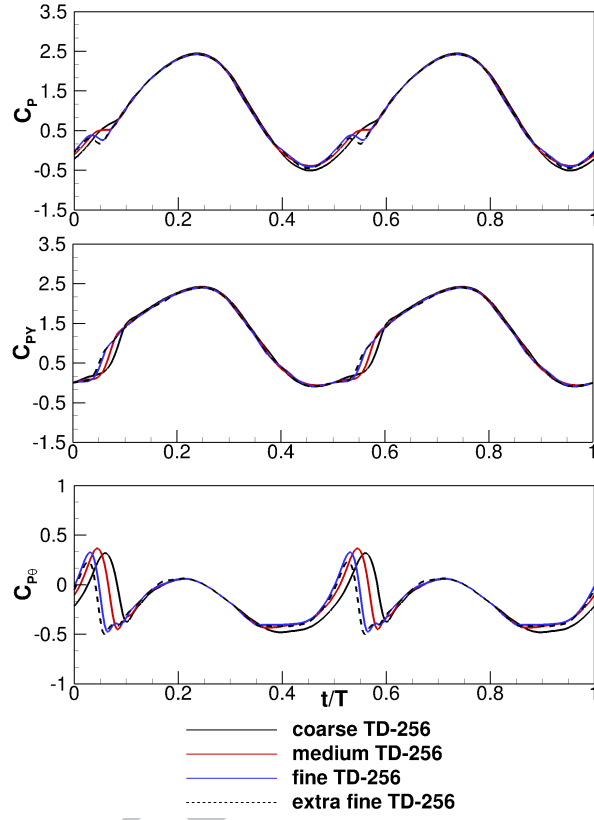


Figure 2: Mesh refinement analysis: overall power coefficient (top), heaving power coefficient (middle), and pitching power coefficient (bottom) obtained using O-grid with coarse, medium, fine and extrafine refinement O-grids.

Such differences become progressively smaller as the time step decreases, and become practically negligible when passing from the $TD - 512$ to the $TD - 1024$ analysis, indicating that 512 intervals per period are sufficient to achieve a solution independent of the time step. Similarly to what was highlighted in the assessment of the effect of the spatial resolution on the computed solution, the differences among the solutions obtained using 128, 256 and 512 steps per cycle are also due to small variations of the timing of the LEVS. These variations rapidly decrease as the grid is refined. The mean values of the power coefficient profiles depicted in Fig. 3 are reported in Tab. 2, along with the efficiency η .

Table 1: Mesh refinement analysis: mean overall, heaving and pitching power coefficients, and energy extraction efficiency η obtained using O-grid with coarse, medium, fine and extrafine refinement O-grids.

refinement	\bar{C}_P	\bar{C}_{P_y}	\bar{C}_{P_θ}	$\eta(\%)$
coarse	1.004	1.176	-0.172	39.19
medium	1.015	1.176	-0.161	39.63
fine	1.011	1.184	-0.173	39.45
extra fine	0.998	1.188	-0.190	38.95

Also in this case, the output featuring the highest sensitivity to the refinement is the mean pitching power.

All 2D time-dependent simulations were performed using the MG solver with 3 grid levels, and a CFL number of 4.
305

Table 2: Time step refinement analysis: mean overall, heaving and pitching power coefficients, and energy extraction efficiency η obtained using 128, 256, 512 and 1024 steps per oscillation cycle.

N_T	\bar{C}_P	\bar{C}_{P_y}	\bar{C}_{P_θ}	$\eta(\%)$
128	0.984	1.149	-0.164	38.41
256	1.004	1.176	-0.172	39.19
512	1.015	1.203	-0.187	39.63
1024	1.016	1.209	-0.191	39.66

The spatial and temporal mesh refinement analyses above highlight that a fully mesh-independent solution is obtained using the 2D fine grid and 512 time intervals per cycle. However, to keep the computational cost of the 3D analyses within the size of the available resources, the 2D coarse grid was chosen as the foil planar mesh of the 3D grid, and 256 time intervals per cycle were used in the 3D simulations reported below. In the light of the findings presented below, however, it is the authors' view that the use of relatively coarse spatial and temporal grids made herein does not significantly affect the main conclusions of the investigations of this report. This aspect is discussed in section 4.
310

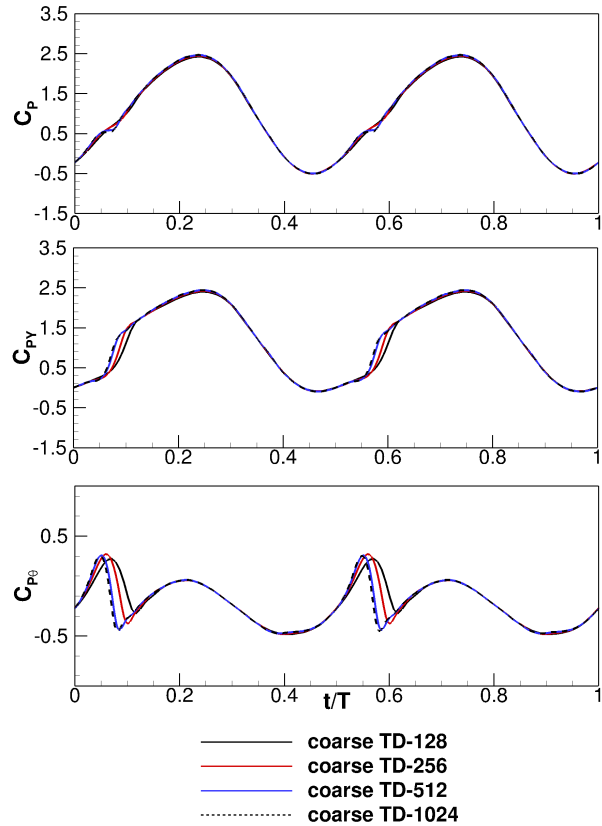


Figure 3: Time step refinement analysis: overall power coefficient (top), heaving power coefficient (middle), and pitching power coefficient (bottom) obtained using 128, 256, 512 and 1024 steps per oscillation cycle.

³¹⁵ The 3D simulations used a symmetry boundary condition at midspan to halve computational costs, and the 3D grid was built by stacking the 2D 256×256 O-grid in the spanwise direction from the midspan symmetry plane to the lateral farfield boundary, which was at 50 chords from the symmetry boundary. The *AR* of the wing was 10. Constant spanwise spacing $\Delta z = 0.02c$ was used from midspan to 90 % semispan, and from here the grid was clustered towards the tip achieving a minimum spacing $\Delta z = 6.4 \times 10^{-6}c$, equal to the minimum distance from the foil surface in the plane of the foil itself. The cell size increased
³²⁰

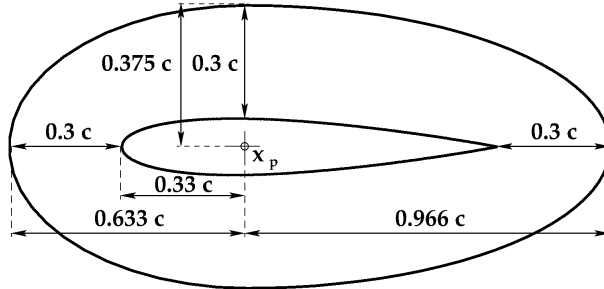


Figure 4: Endplate geometry.

again moving from the tip to the lateral farfield boundary. The grid featured 244 cells between the symmetry plane and the wing tip, and 144 cells between the wing tip and the lateral farfield boundary. The complete grid had about 30.7 million cells.

Two wing tip topologies were considered, one with sharp tips, the other with endplates. The geometry of the endplate is depicted in Fig. 4. Careful grid design enabled the use of the same grid for both configurations, removing all uncertainty in the comparative analysis of these two configurations arising from using different grid topologies. A view of the surface mesh of the two 3D grids is provided in Fig. 5. In all simulations presented in this study, the minimum nondimensional wall distance y^+ was found to be smaller than one at all times of the periodic flow field.

The CFL number of both the simulation of the wing with sharp tips and that of the wing with endplates was set to 3. Due to numerical instabilities encountered with the MG solver, both simulations were run using a single grid level. CFL ramping was used for all time steps, and 2,800 iterations were performed to compute the solution of each physical time. With this set-up, the residuals of the NS equations decreased by about 4 orders of magnitude at all physical times, and all force and moment components fully converged within 2,500 iterations. For both 2D and 3D analyses, the number of oscillation cycles typically required to achieve the 0.1 % periodicity error threshold on C_Y varied

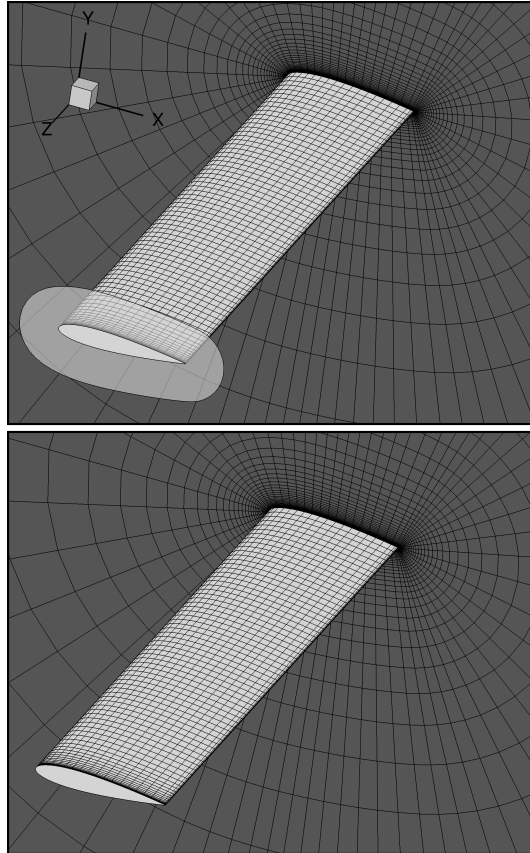


Figure 5: Surface mesh of wing and symmetry boundary (only every fourth grid line in all directions is reported). Top: wing with endplate. Bottom: wing with sharp tip.

between four and ten, depending on the spatial and temporal refinement, and
³⁴⁵ also on whether the simulation had been started from a freestream condition or from the solution of a simulation using the same grid but different temporal refinement.

4.2. hydrodynamic analysis

The infinite- and finite-span oscillating wing configurations analyzed herein
³⁵⁰ share the same trajectory, which corresponds to that defined in the previous subsection. The evolution of the main kinematic parameters of all wings over one

oscillation cycle is depicted in Fig. 6. The plot shows the time-dependent values of the vertical position h of the wing, its angular position θ , the nondimensionalized heaving velocity v_y/u_∞ , and the nondimensionalized pitching velocity Ω/Ω_{max} , with Ω_{max} being the maximum pitching velocity of the cycle. The figure also reports the effective AoA α computed with Eq. (3). One notes that the maximum AoA is about 35° . The four positions labeled 1 to 4 correspond to 5%, 15%, 25% and 35% of the period respectively, and are those at which the flow field is examined in greater detail in the following analyses.

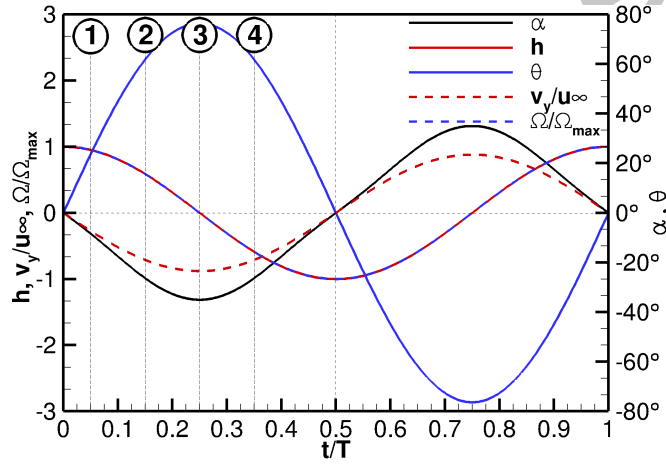


Figure 6: Kinematic parameters of the trajectory of the infinite- and finite-span wings.

The main integral performance metrics of the infinite wing, the *AR* 10 wing with endplates (EPs) and the *AR* 10 wing with sharp tips (STs) are reported and compared in Table 3. Columns 2 to 4 provide respectively the mean values of the overall power coefficient \bar{C}_P , the heaving power coefficient \bar{C}_{P_y} , and the pitching power coefficient \bar{C}_{P_θ} ; column 5 provides the overall efficiency η , whereas the percentage variations (Δs) of the three mean power coefficients of the *AR* 10 wings with respect to the reference values of the infinite wing are reported in columns 6 to 8. The infinite wing analysis is based on the 2D coarse grid *TD* – 256 simulation, whereas the two *AR* 10 analyses are based on fully 3D *TD* – 256 simulations using the 30.7 million-cell grid described above. One

³⁷⁰ notes that \bar{C}_P of the $AR\ 10$ wing with EPs is 12.4 % lower than that of the infinite wing, whereas \bar{C}_P of the $AR\ 10$ wing with STs is nearly 17 % lower than that of the ideal infinite wing. The breakdown of the overall mean power into heaving and pitching power components for the three cases highlights that: *a)* the mean negative pitching power (a loss term) of both $AR\ 10$ wings increases by the same amount with respect to the ideal infinite wing case (about 39 %),
³⁷⁵ *b)* the heaving power coefficient of both $AR\ 10$ wings decreases with respect to that of the infinite span wing: by about 4.9% for the wing with EPs, and by about 8.7% for the wing with STs. These observations highlight that 3D flow effects hit the overall energy extraction efficiency of this device in a complex manner, that appears not to depend only on the geometry of the wing tips.

Table 3: Integral performance metrics of infinite wing and two $AR\ 10$ wings. Columns 2 to 4: mean overall, heaving and pitching power coefficients; column 5: energy extraction efficiency η ; columns 6 to 8: percentage variations of overall, heaving and pitching power coefficients of two $AR\ 10$ wings with respect to infinite wing values.

AR	\bar{C}_P	\bar{C}_{P_y}	\bar{C}_{P_θ}	$\eta(\%)$	$\Delta\bar{C}_P(\%)$	$\Delta\bar{C}_{P_y}(\%)$	$\Delta\bar{C}_{P_\theta}(\%)$
∞	1.004	1.176	-0.172	39.19	-	-	-
10 EP	0.879	1.118	-0.239	34.32	-12.4	-4.9	-38.9
10 ST	0.835	1.074	-0.239	32.58	-16.8	-8.7	-38.9

³⁸⁰

The top subplot of Fig. 7 reports the C_P profiles of the three wings over one period, whereas the bottom subplot reports their C_{P_y} and C_{P_θ} profiles. In the first 10 % and last 15 % of both semi-periods (region 1), the $AR\ 10$ C_P profiles are superimposed and are significantly lower than that of the infinite wing. The ³⁸⁵ C_P profiles of the $AR\ 10$ wings are lower than that of the infinite wing also in the remainder of the cycle (region 2), but the profile of the wing with EPs is higher than that of the wing with STs. The profiles of the pitching and heaving power coefficients in the bottom subplot of Fig. 7 show that in region 1 an increment of the heaving power of the two $AR\ 10$ wings with respect to the infinite wing is outweighed by a larger reduction of their pitching power. This explains why the ³⁹⁰ profiles of the overall power coefficient of the finite span wings in region 1 are

lower than that of the infinite wing. In region 2 the pitching power of all three wings is comparable, and the lower overall power of the two *AR* 10 is caused primarily by a reduction of the heaving power component, which is greater for the wing with STs.

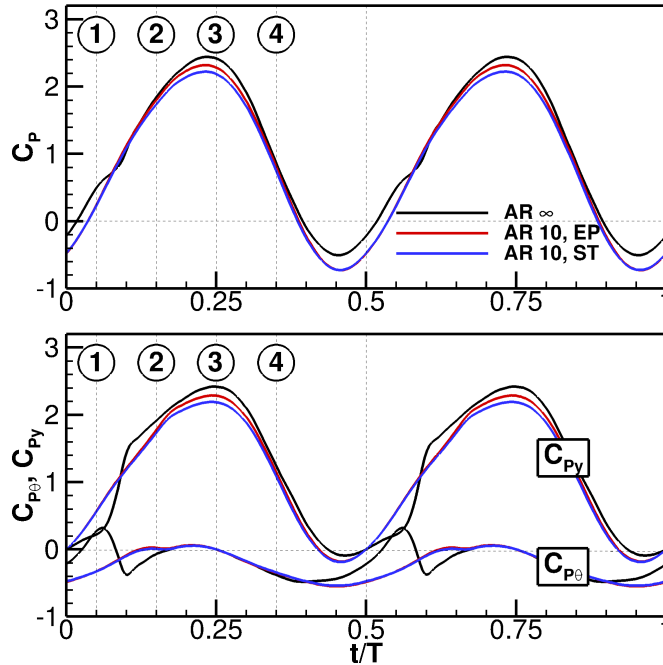


Figure 7: Overall power coefficient (top), heaving power coefficient (middle), and pitching power coefficient (bottom) of infinite wing and two *AR* 10 wings.

395

To further investigate the dependence of the energy extraction efficiency of the finite span wing on the tip geometry highlighted by Table 3 and Fig. 7, the periodic profiles of the heaving power coefficient per unit wing length $C_{P_{zy}}$ and the pitching power coefficient per unit length $C_{P_{z\theta}}$ of the *AR* 10 wings
 400 are cross compared at five spanwise positions in Fig. 8, which also reports the infinite wing profiles for reference. Between about 18 % and 50 % of both semi-periods, the heaving power coefficient of both finite wings from midspan to about 60 % semispan is only negligibly smaller than the corresponding infinite wing profile. It is observed, however, that throughout the period this power

component decreases much more rapidly with respect to the ideal case from 60 % semispan to the tip region (95 % semispan) when the finite wing has STs. This performance difference is due mainly to the existence of stronger tip vortices featured by the finite wing without EPs. Consequently, the downwash lowering the effective AoA with a strength decreasing from tip to midspan is higher for the ST-wing. Note also that the largest differences between the heaving power of the finite span wings occur in the period range with maximum nominal AoA. The comparison of the $C_{P_{z\theta}}$ profiles of the three wings reported in Fig. 8 highlights several important phenomena. Firstly, the wing tip geometry does not appear to have a significant effect on the pitching power component of the two finite span wings, since the $C_{P_{z\theta}}$ profiles of the two AR 10 wings are extremely close at all reported spanwise positions. Secondly, although the pitching power profiles of both wings between about 18 % and 35 % of both semi-periods coincide with the infinite wing profile at all reported spanwise positions, substantial qualitative and quantitative differences between the two finite wing and the infinite wing profiles exist over the remainder of the cycle at all spanwise locations. The infinite wing pitching power profile features a marked positive peak at about 6 % of both semi-periods, whereas at midspan of both AR 10 wings such peak has moved to about 14 % of the semi-period with greatly reduced strength. As one moves towards the wing tip, the peak disappears completely. As shown below, these important performance differences between the infinite and the finite wings are caused by a loss of favourable synchronization between pitching motion and LEVS affecting the latter wings. It is also noted that the complete disappearance of the pitching power peak at the outboard sections of both finite wings in the first 20 % of the semi-periods occurs because LEVS rapidly decreases from about 60 % semispan to the wing tip.

The vortex indicator λ_2 defined in [19] is used herein to visualize the flow patterns at the tips of the two finite wings. The isosurface $\lambda_2 = -0.1$ in the tip region of the wing with endplates and that in the tip region of the wing with sharp tips at 25 % of the oscillation cycle are shown in Fig. 9-a and Fig. 9-b respectively. The pattern of the λ_2 isosurface at the sharp tips, indicates

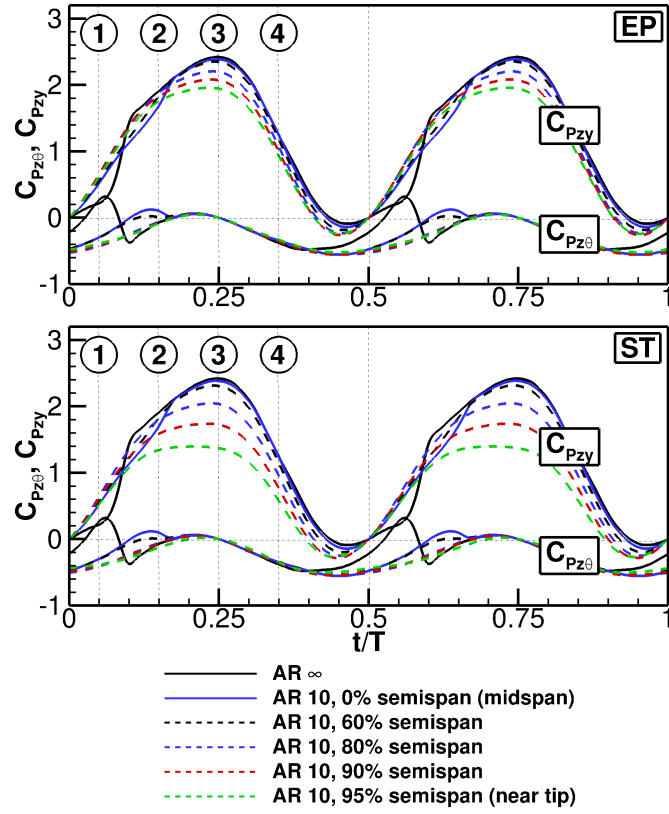


Figure 8: Overall power coefficient per unit wing length (top), heaving power coefficient per unit wing length (middle), and pitching power coefficient per unit wing length (bottom) of infinite wing and two $AR = 10$ wings at seven spanwise positions.

that vorticity from the pressure side rolls down to the suction side to form a trailing vortex, which causes the downwash effect. The downwash leads to the aforementioned reduction of the effective AoA at the sections close to the tip, reducing C_{P_y} , as observed in the bottom plot of Fig. 8. The top plot of Fig. 9 shows that a tip vortex also exists for the wing with endplates. This vortex, however, originates at the edge of the endplate and is farther away from the wing than the vortex of the wing with sharp tips, resulting in less pronounced downwash. Moreover the vortex originating at the endplate is weaker than that

originating at the sharp tip, because the driving pressure difference is smaller in the former case.

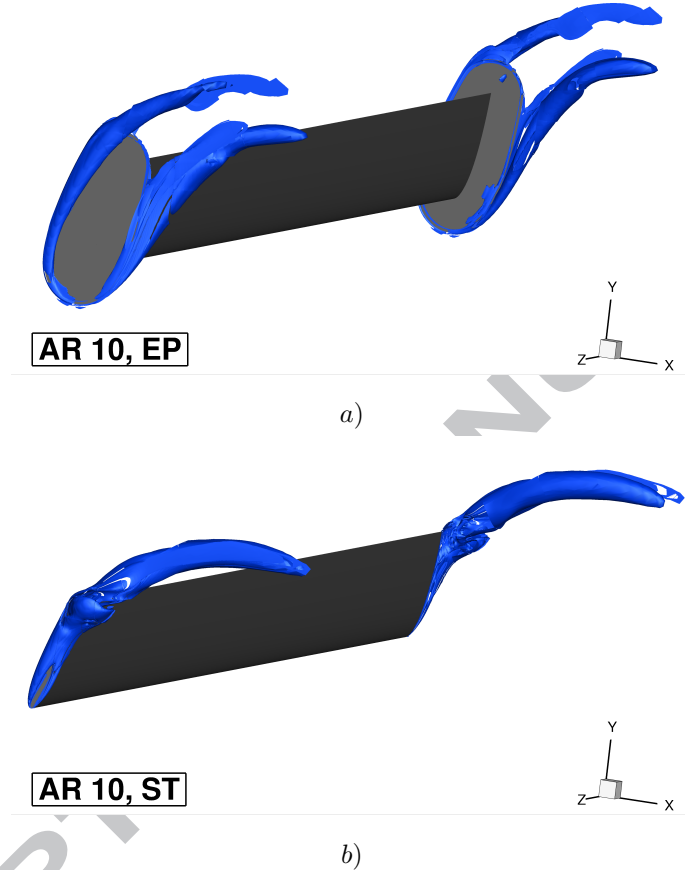


Figure 9: Isosurface of vortex indicator $\lambda_2 = -0.1$ at 25 % of cycle (position 3 in Fig. 6) for a) wing with endplates, and b) wing with sharp tips.

445

The comparison of the skin friction lines of the two finite span wings at 25 % of the vertical stroke from 50 % semispan to tip are reported in Fig. 10. The skin friction lines on the pressure side (PS) and suction side (SS) of the wing with EPs are depicted in the top left and bottom left subplots respectively, whereas those of the wing featuring STs are reported in the right subplots. One sees that the use of endplates results in the stream being much better guided and kept aligned with the wing chord. This is highlighted by the fact that the skin

450

friction lines on the outboard portion of the wing have a more rectilinear path when using endplates. In the same region, conversely, the skin friction lines on the pressure side of the wing with STs deviate towards the tip rather than progressing towards the trailing edge (TE). This pattern denotes the local flow motion towards the tip where a strong tip vortex is formed. The comparison of the PS flow patterns (top subplots) of the two wings also shows that the stagnation line at the corner between the LE and the wing tip is closer to the LE in the case of the ST-wing. This is due to stronger downwash hitting the ST-wing, which reduces the lift force and thus the amount of work the near-tip sections can extract from the fluid stream. The bottom left subplot also shows a small 3D recirculation region on the wing SS at the corner between the wing endplate and the wing trailing edge. This denotes the existence of a corner stall region similar to that encountered in shrouded turbomachinery rotors and stators [20].

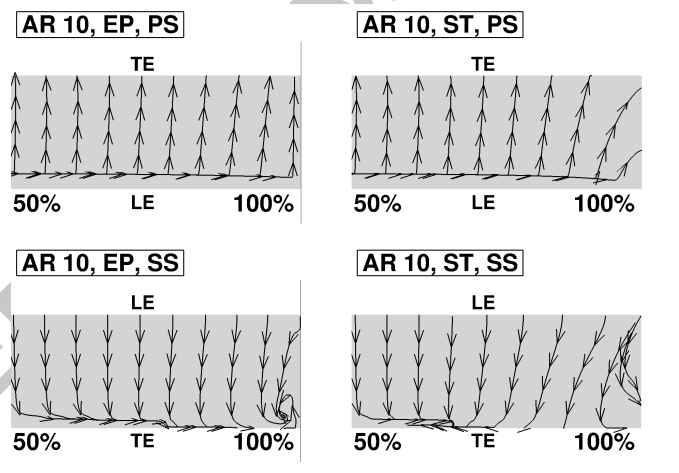


Figure 10: Skin friction lines on pressure side (PS) and suction side (SS) of wing with sharp tips and endplates at 25% of cycle (position 3 in Fig. 6).

Contour slices of the z component of the flow vorticity at thirteen spanwise positions of the EP-enhanced wing, the ST-wing and the infinite wing at 5 % of the oscillation cycle (position 1) are reported respectively in the left, middle and

right images of Fig. 11. Inspection of the vorticity contours of the two $AR = 10$ wings reveals that the only significant difference between these two configurations is the presence of the footprint of the tip vortex behind the trailing edge of the tip section of the wing with sharp tips. Moreover, for both wings the vortex associated with LEVS (blue vorticity region on the wing PS) is absent in the near-tip region, indicating a strong loss of coherent vortical structure due to finite wing effects. The comparison of the vorticity contours of the two $AR = 10$ wings and the infinite wing highlights that the vortex associated with finite wings LEVS lags behind that of the infinite wing. This phase difference has an important effect on the variations of the generated power of the finite wings relative to the infinite wing, due to different static pressure fields on the wing surface.

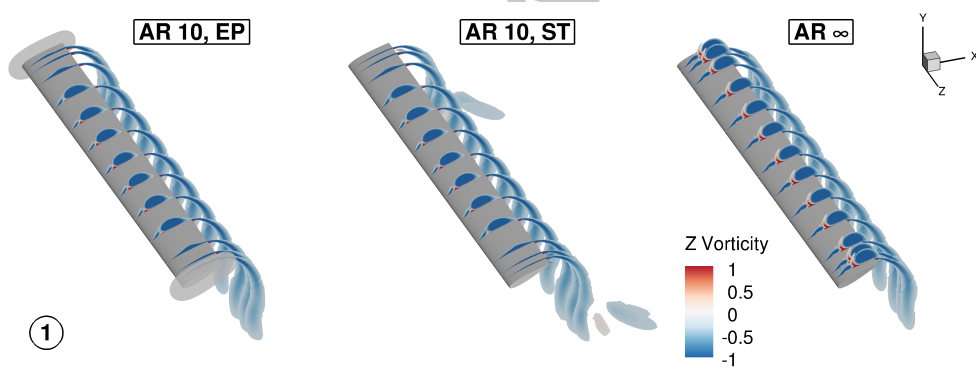


Figure 11: Contours of z component of flow vorticity along wing span at 5 % of cycle (position 1 in Fig. 6). Left: wing with EPs; middle: wing with STs; right: infinite wing.

Figure 12 provides the contour slices of the pressure coefficient c_p at the same spanwise positions of the three wings and the same point of the cycle used in Fig. 11. The definition of c_p is:

$$c_p = \frac{p - p_\infty}{\frac{1}{2} \rho_\infty u_\infty^2} \quad (9)$$

where p and p_∞ denote local and freestream static pressure respectively. The blue color in all three images corresponds to the low-pressure region associated

with the passage of the high-kinetic energy vortex. It is observed that the low-pressure region on the top side of the infinite wing is wider than in the other two configurations, and, more importantly, it is farther away from the pitching center (*i.e.* closer to the TE). This results in a larger upward force acting on the rear of the infinite wing, and, in turn, in a higher positive (counterclockwise) pitching moment. At this time of the period, the angular velocity of all wings is also positive and close to its maximum, as visible in Fig. 6. As a result, the pitching power of the infinite wing is higher than that of the two finite span wings in their midspan region. This is the reason why Fig. 8 shows that the peak of the pitching power of the infinite wing in the first 20 % of the semi-periods is significantly higher than that of the midspan sections of the AR 10 wings in the same region of the cycle. On the other hand, the wider extent of the low-pressure area on the top side of the infinite wing, due to a stronger vortex intensity, results in a reduction of the downward heaving force and, in turn, a reduction of the heaving power at this point of the cycle. For the opposite reason, the AR 10 wings have higher heaving power in this region of the cycle. As observed before, however, such higher heaving power is outweighed by the loss of pitching power. In the light of these phenomena, it can be concluded that the loss of favorable synchronization between LEVS and pitching motion with respect to the infinite wing case results in a significant total power loss that is largely independent of the wing tip geometry.

Contour slices of c_p at thirteen spanwise positions of the three wings at 25 % of the oscillation cycle (position 3) are reported respectively in the left, middle and right images of Fig. 13. No differences among the static pressure field of the three wings is observed from midspan to more than 60 % of the semispan. In the tip region of both AR 10 wings, however, the static pressure on the top side is lower than for the infinite wing. This is due to the tip load reductions associated with the formation of the tip vortex, and results in a smaller downward force and heaving power. As expected, this loss depends on the tip geometry, as highlighted by the fact that the pressure acting on the top side of the EP-enhanced wing in the tip region is higher than that of the

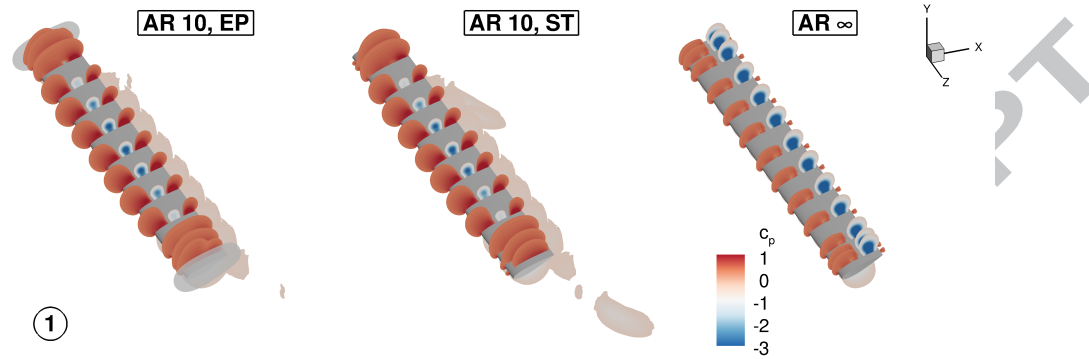


Figure 12: Contours of pressure coefficient along wing span at 5 % of cycle (position 1 in Fig. 6). Left: wing with EPs; middle: wing with STs; right: infinite wing.

ST-wing.

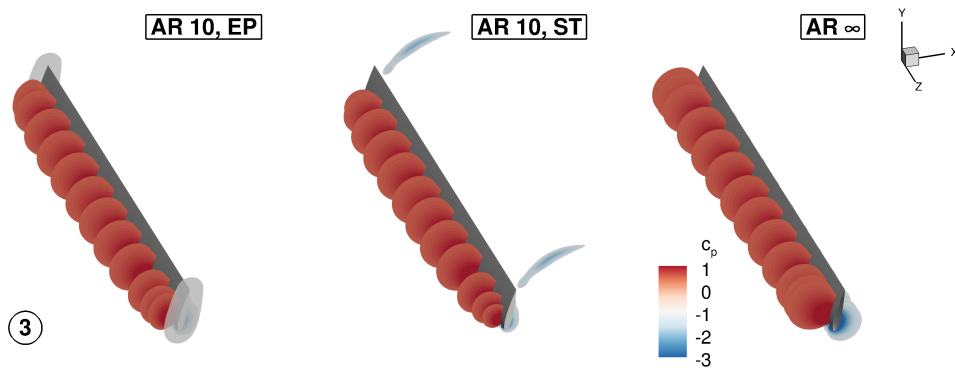


Figure 13: Contours of pressure coefficient along wing span at 25 % of cycle (position 3 in Fig. 6). Left: wing with EPs; middle: wing with STs; right: infinite wing.

The effects of the flow mechanisms discussed above are examined in a more quantitative fashion in Figures 14 and 15. The former provides the foil static pressure coefficient at midspan for the three wings at the positions labeled 1 to 4 in Fig. 6; the latter has the same structure but refers to the wing section at 95 % semispan. Inspection of the results of Fig. 14 confirms that neither qualitative nor quantitative differences exist between the flow pattern of the

525 two $AR = 10$ wings at midspan, indicating that for this value of AR the performance of the midspan region is fairly independent of the wing tip geometry. At position 3, where the effects of LEVS are absent, the flow of the two finite wings is virtually two-dimensional, as indicated by the fact that all three profiles are superimposed. At positions 1 and 4, conversely, the infinite and finite
 530 wing c_p profiles differ substantially due to different patterns of the LEVS. This, as discussed, results in lower overall power generation of the $AR = 10$ wings. At position 2 the relatively small differences between the infinite and the finite wings are due to effects of the delayed vortex being still perceived by the finite wings. The four subplots of Fig.15 highlight the significant effect of tip design
 535 on the hydrodynamic performance of the oscillating wing. It is observed that the loading of the near-tip section, here taken as the area between the SS and PS of the wing, is higher when using EPs, due to the lower downwash caused by a weaker tip vortex pattern. The performance difference associated with the use of either tip geometry is particularly strong between positions 1 and 3, which define the interval in which the effective AoA ramps up towards its maximum.
 540

4.3. discussion

The 12.4 % reduction of the overall mean power coefficient of the $AR = 10$ endplate-enhanced wing with respect to the infinite wing (Tab. 3) is comparable to the 11 % reduction of the same wing reported by Kinsey and Dumas [12].
 545 It should be noted, however, that significant differences between the analyses yielding the two efficiency loss estimates exist. The present simulation used a 30.7 million structured multi-block grid, the SST turbulence model, a Reynolds number of 1.5 million and a pitching amplitude of 76.3° ; the analysis of [12] used a 3.4 million unstructured grid, the Spalart-Allmaras turbulence model, a
 550 Reynolds number of 0.5 million and a pitching amplitude of 75.0° . The closeness of the two results makes one wonder if the outcome of the comparative analysis of this paper would vary fairly little for Reynolds number between 0.5 and 1.5 million. Answering this question with confidence is presently hard due to the lack of the analysis of the $AR = 10$ wing with sharp tips in the study of [12]

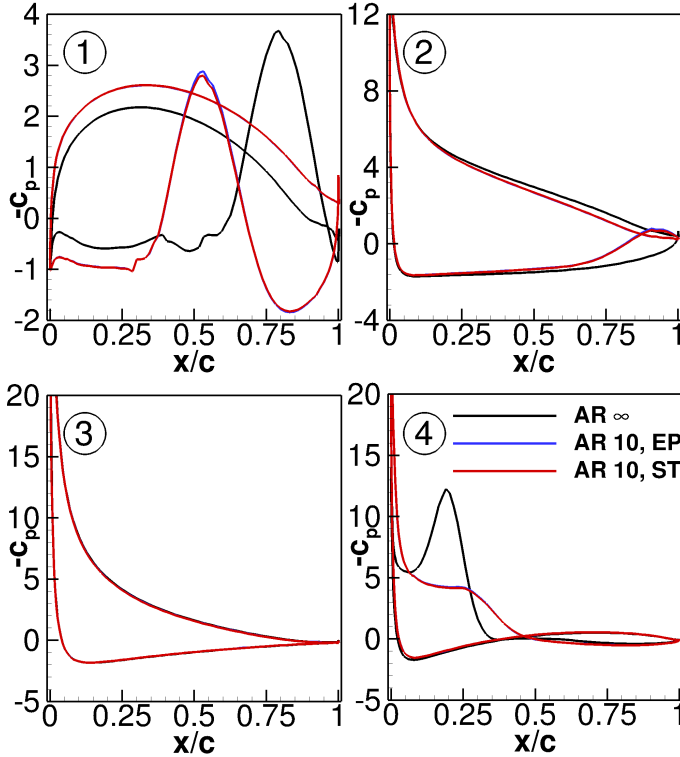


Figure 14: Pressure coefficient c_p of infinite wing, and at midspan of $AR\ 10$ wings at positions labeled 1 to 4 in Fig. 6.

and also the aforementioned differences of the computational approach. It is also noted that the article [12] provides the comparative analysis of the finite wings with sharp tips and endplates for $AR\ 5$ and 7 . Although the overall loss levels for these configurations are higher than for $AR\ 10$ (as expected), the qualitative differences of flow patterns of the two wing types for given aspect ratio appear to be similar to those observed in the present study. This may point to independence of the qualitative aspects of the present analysis on the Reynolds number for $0.5 \times 10^6 < Re < 1.5 \times 10^6$.

The COSA code adopted for the analysis of this study is compressible, and therefore it requires prescribing the free stream Mach number on all far field boundaries. The free stream Mach number was set to 0.1, and this choice

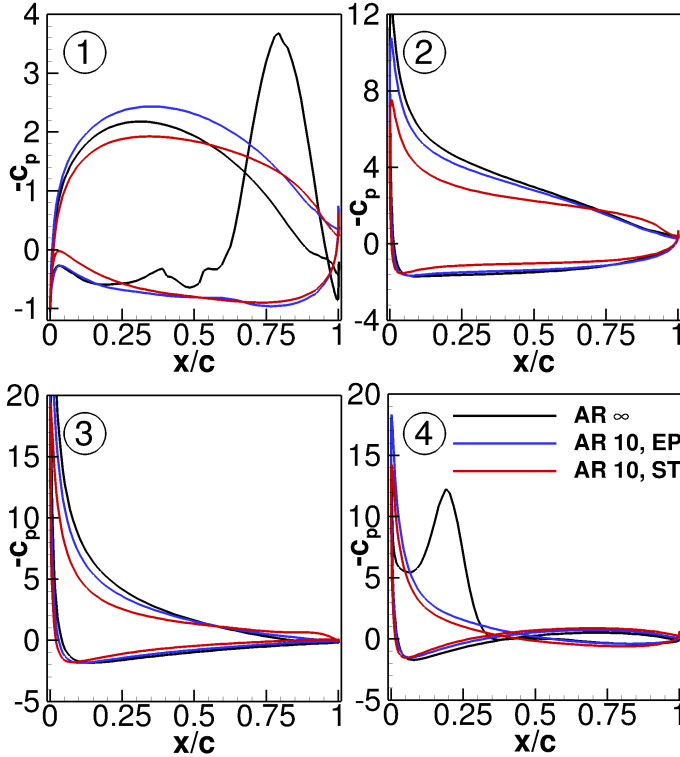


Figure 15: Pressure coefficient c_p of infinite wing, and at 95 % semispan section of $AR\ 10$ wings at positions labeled 1 to 4 in Fig. 6.

resulted in the maximum relative Mach number in the flow field never exceeding 0.3, the threshold above which compressibility effects may appear. Hence, the presented analyses do not include compressibility effects.

Arguably, the use of relatively coarse spatial and temporal discretizations (coarse base 2D grid and 256 time-intervals per period) made herein might have introduced some uncertainty in the quantitative estimates of the results discussed above. More precise quantification of the variations of the power coefficients with the wing AR and tip design may require larger grids and computational resources. Nevertheless, the authors' view is that a higher resolution is unlikely to alter significantly the general findings of the analyses above, particularly the key ones on the loss of optimal synchronization between LEVS

and wing motion, and the consequent efficiency loss of both finite-span wings with respect to the infinite wing. Considering the case of the pitching power profile, this is because its variation with the spatial and temporal refinement in the 2D analysis (Figures 2 and 3) consists mainly of relatively small shifts of its peak values due to small variations of the phase between LEVS and foil motion, and does not correspond to any significant variation of LEVS vortical structures (these analyses have not been included for brevity). Conversely, the pitching power profile of the 3D wings on one hand and the infinite-wing on the other have substantially different patterns. (Figures 7 and 8). Such pattern alterations are due to variations of the phase between LEVS and wing motion which are much larger than those due to varying spatial and temporal refinement. Moreover, the efficiency loss of the two finite-span wings appears to be fairly independent of the tip geometry (column 8 of Table 3), which makes one assume that a higher refinement of the tip region flows is unlikely to change the important physical finding on the loss of optimal synchronization between LEVS and wing motion due to finite-wing effects. Such a higher refinement may instead be advisable for further verification of the quantitative dependence of the efficiency loss on the tip geometry.

595 5. Conclusions

A detailed numerical investigation into the impact of flow three-dimensionality on the power generation efficiency of realistic oscillating wing configurations for renewable energy production has been presented. The study was based on the comparative performance assessment of an infinite wing and two aspect ratio 10 wings, one featuring endplates, the other featuring sharp tips. The oncoming stream had $Re = 1.5 \times 10^6$; the wing motion was characterized by a fairly high power generation efficiency of the infinite wing at this Reynolds number and the occurrence of fairly well timed LEVS. The COSA RANS research code featuring Menter's SST turbulence model was used to assess the differences of hydrodynamic performance of the three configurations and analyze the under-

lying flow patterns accounting for such differences. Computational grids with 30.7 million-cells were used for the 3D time-dependent simulations.

The mean overall power coefficient of the *AR* 10 wing with sharp tips and endplates are found to decrease respectively by about 17 % and 12 % with respect to that of the infinite wing. The finite wing losses are caused both by the reduction of the effective AoA at the near-tip sections induced by the downwash associated with the tip vortices, and the loss of optimal synchronization of LEVS and pitching motion of the wing. The latter phenomenon results in a lower efficiency of the finite span wing due to a significant loss of pitching power with respect to the ideal infinite wing.

The loss due to tip vortex-induced downwash depends on the wing tip geometry, and is smaller for the wing with endplates. The pitching power loss, however, does not depend on the wing tip geometry, and hits in a qualitatively and quantitatively similar fashion both *AR* 10 wings.

A recent optimization study aiming at determining combinations of kinematic parameters (oscillation frequency, heaving and pitching amplitudes) to maximize the energy capture efficiency highlighted that high efficiency levels can be achieved also with kinematic conditions which do not yield LEVS [14]. In the light of the efficiency reduction associated with the loss of favorable synchronization between pitching motion and LEVS when considering finite wing effects, it appears advisable to design these devices avoiding regimes characterized by 2D LEVS, so as to minimize losses due to finite wing effects. Alternatively one would have to perform the design optimization of the wing kinematic parameters making use of costly 3D flow simulations, since the results of 2D optimization appear to be unsuitable to yielding optimal efficiency of the 3D oscillating wing.

Acknowledgements

The analyses reported in this paper made use of the ARCHER UK National Supercomputing Service and the Hartree Centre computing resources.

635 The STFC Hartree Centre is a collaborative research programme in association
 with IBM providing High Performance Computing platforms funded by
 the UK's investment in e-Infrastructure.

References

- [1] W. McKinney, J. DeLaurier, The Wingmill: An Oscillating-Wing Windmill, Journal of Energy 5 (1) (1981) 109–115.
 640
- [2] K. Jones, K. Lindsey, M. Platzer, An Investigation of the Fluid-Structure Interaction in an Oscillating-Wing Micro-Hydropower Generator, in: Chakrabarti, Brebbia, Almozza, Gonzalez-Palma (Eds.), Fluid Structure Interaction 2, WIT Press, Southampton, United Kingdom, 2003, pp. 73–
 645 82.
- [3] J. Young, J. Lai, M. Platzer, A review of progress and challenges in flapping foil power generation, Progress in Aerospace Sciences 67 (2014) 2–28.
- [4] Q. Xiao, Q. Zhu, A review of flow energy harvesters based on flapping foils, Journal of Fluids and Structures 46 (2014) 174–191.
- 650 [5] Q. Xiao, W. Liao, S. Yang, Y. Peng, How motion trajectory affects energy extraction performance of a biomimic energy generator with an oscillating foil?, Renewable Energy 37 (2012) 67–75.
- [6] I. Fenercioglu, B. Zaloglu, J. Young, J. Lai, M. Platzer, Flow Structures Around an Oscillating-Wing Power Generator, AIAA Journal 53 (11)
 655 (2015) 3316–3326.
- [7] T. Kinsey, G. Dumas, Parametric Study of an Oscillating Airfoil in a Power-Extraction Regime, AIAA Journal 46 (6) (2008) 1318–1330.
- [8] M. Campobasso, J. Drofelnik, Compressible Navier-Stokes analysis of an oscillating wing in a power-extraction regime using efficient low-speed preconditioning, Computers and Fluids 67 (2012) 26–40.
 660

- [9] T. Kinsey, G. Dumas, G. Lalande, J. Ruel, A. Mehut, P. Viarogue, J. Lemay, Y. Jean, Prototype testing of a hydrokinetic turbine based on oscillating hydrofoils, *Renewable energy* 36 (2011) 1710–1718.
- [10] T. Kinsey, G. Dumas, Computational Fluid Dynamics Analysis of a Hydrokinetic Turbine Based on Oscillating Hydrofoils, *Journal of Fluids Engineering* 134 (2012) 021104.1–021104.16.
- [11] P. Spalart, S. Allmaras, A one-equation turbulence model for aerodynamic flows, *La Recherche Aerospaciale* 1 (1994) 5–21.
- [12] T. Kinsey, G. Dumas, Three-Dimensional Effects on an Oscillating-Foil Hydrokinetic Turbine, *Journal of Fluids Engineering* 134 (2012) 071105.1–071105.11.
- [13] M. Campobasso, A. Piskopakis, J. Drofelnik, A. Jackson, Turbulent Navier-Stokes Analysis of an Oscillating Wing in a Power-Extraction Regime Using the Shear Stress Transport Turbulence Model, *Computers and Fluids* 88 (2013) 136–155.
- [14] T. Kinsey, G. Dumas, Optimal Operating Parameters for an Oscillating Foil Turbine at Reynolds Number 500,000, *AIAA Journal* 52 (9) (2014) 1885–1895.
- [15] F. Menter, Two-equation Turbulence-models for Engineering Applications, *AIAA Journal* 32 (8) (1994) 1598–1605.
- [16] A. Betz, Das Maximum der Teoretisch Möglichen Ausnützung des Windes Durch Windmotoren, *Zeitschrift für das Gesamte Turbinenwesen* 20 (1920) 307–309.
- [17] M. Campobasso, F. Gigante, J. Drofelnik, Turbulent Unsteady Flow Analysis of Horizontal Axis Wind Turbine Airfoil Aerodynamics Based on the Harmonic Balance Reynolds-Averaged Navier-Stokes Equations, ASME paper GT2014-25559 (June 2014).

- [18] A. Jackson, M. Campobasso, Shared-memory, Distributed-memory and Mixed-mode Parallelization of a CFD Simulation Code, Computer Science Research and Development 26 (3-4) (2011) 187–195.
690
- [19] J. Jeong, F. Hussain, On the identification of a vortex, Journal of Fluid Mechanics 285 (1995) 69–94.
- [20] M. Campobasso, A. Mattheiss, U. Wenger, A. Arnone, P. Boncinelli, Complementary Use of CFD and Experimental Measurements to Assess the Impact of Shrouded and Cantilevered Stators in Axial Compressors, ASME paper 99-GT-208 (June 1999).
695

highlights.txt

Assessed renewable energy generation potential of finite-span oscillating wings

Examined hydrodynamics of finite-span oscillating wings with sharp tips and endplates

Used three-dimensional turbulent time-dependent simulations with 30,000,000-cell grid

Power loss of wing with sharp tips amounts to about 17 percent of infinite wing power

Power loss of wing with endplates amounts to about 12 percent of infinite wing power